RESEARCH ARTICLE

Comparative numerical modeling of inhaled micron-sized particle deposition in human and rat nasal cavities

Yidan Shang, Jingliang Dong, Kiao Inthavong, and Jiyuan Tu

School of Aerospace, Mechanical & Manufacturing Engineering, and Platform Technologies Research Institute (PTRI), RMIT University, Bundoora, VIC, Australia

Abstract

Micron-sized particle deposition in anatomically realistic models of a rat and human nasal cavity was numerically investigated. A steady laminar inhalation flow rate was applied and particles were released from the outside air. Particles showing equivalent total particle deposition fractions were classified into low, medium and high inertial particle. Typical particle sizes are 2.5, 9 and 20 µm for the human model and 1, 2 and 3 µm for the rat model, respectively. Using a surface-mapping technique the 3D nasal cavity surface was "unwrapped" into a 2D domain and the particle deposition locations were plotted for complete visual coverage of the domain surface. The total surface area comparison showed that the surface area of the human nasal model was about ten times the size of the rat model. In contrast, the regional surface area percentage analysis revealed the olfactory region of the rat model was significantly larger than all other regions making up ∼55.6% of the total surface area, while that of the human nasal model only occupying 10.5%. Flow pattern comparisons showed rapid airflow acceleration was found at the nasopharynx region and the nostril region for the human and rat model, respectively. For the human model, the main passage is the major deposition region for micro-particles. While for the rat model, it is the vestibule. Through comparing the regional deposition flux between human and rat models, this study can contribute towards better extrapolation approach of inhalation exposure data between inter-subject species.

Introduction

To evaluate the health risk by inhalation exposure, particle dosimetry models have been developed to predict the fate of inhaled airborne particles in the respiratory passages (Asgharian et al., 2014; Kelly et al., 2005). This requires information regarding the amount of particles escaping from the nasal cavity. Particles that deposit onto the nasal cavity have two possible uptake routes. They can cross the respiratory epithelium and reach the underlying blood vessels, or be adsorbed through the olfactory epithelium, transporting along the olfactory bulb and reach the brain, as demonstrated in rat subjects (Bai et al., 2010; Oberdorster et al., 2004). The relevance of this data can be difficult to extrapolate to human subjects because of the different anatomical geometry—in humans the olfactory mucosa represents 5–10% of the total nasal mucosa but 50% in rats (Schroeter et al., 2008).

Early *in vivo* studies of ultrafine particle deposition in rats using exposure chambers include Wolff et al. (1984) and Gerde et al. (1991). Later, Kelly et al. (2001a, 2002) investigated particle deposition fraction in rats where all particles were either directly inhaled or particles were inhaled naturally using head-only units and whole body chambers. The deposition fractions varied between the inhalation methods tested, since particle inhalability inherently differs for each method. This suggests that the breathing region and external nose should be considered in model studies. *In vitro* experiments using replica molds have also received intensive research efforts which investigated the influence of the human nasal cavity (Cheng et al., 1996; Dai et al., 2007; Golshahi et al., 2011) and the rat nasal cavity (Ahmed et al., 2012; Cheng et al., 1990; Kelly et al., 2001b) morphology on particle deposition.

Computational fluid dynamics (CFD) modeling studies have determined airflow patterns, gas uptake and particle deposition in rats (Garcia & Kimbell, 2009; Jiang & Zhao, 2010; Schroeter et al., 2012; Wei et al., 2013), and humans (Dastan et al., 2014; Ghahramani et al., 2014; Ghalati et al., 2012; Inthavong et al., 2008; Oldham, 2000). These studies revealed the main deposition sites for different particle sizes, and used non-dimensional numbers (i.e. inertial parameter, Stokes number, and Peclet number) to incorporate the influence of particle size with combinations of flow rate and airway geometry.

Interspecies modeling comparisons have been performed by Zhao et al. (2006) investigating the influence of sniffing conditions on odorant transport; Schroeter et al. (2008)

Address for correspondence: Prof. Jiyuan Tu, School of Aerospace, Mechanical & Manufacturing Engineering, and Platform Technologies Research Institute (PTRI), RMIT University, PO Box 71, Bundoora, VIC 3083, Australia. Tel: +61-3-9925-6191. Fax: +61-3-9925-6108. E-mail: jiyuan.tu@rmit.edu.au

studying acrolein uptake; and Corley et al. (2012) which considered high-resolution models of the respiratory airway from nose to deep lung branches for vapor uptake analysis.

Although inhaled particle deposition characteristics have been considerably studied both experimentally and numerically, limitations still exist in terms of deposition analysis and data extrapolation among species. The nasal cavity is an extremely complicated geometry that is difficult to visualize without a 3D viewer. This makes particle deposition patterns in nasal cavities inaccessible in some regions. Furthermore, the anatomical geometries of the nasal cavity differ among species causing different fluid–particle interactions and leading to different deposition regions for the same particle sizes.

This study aims to provide detailed particle deposition characteristics of micron-sized particles within anatomically accurate rat and human nasal passages, to reveal their deposition similarities and differences. Unlike previous studies, this article presents a systematic method to visualize the respiratory surface by converting the 3D nasal cavity surface into a 2D domain. This allows data access to the entire wrapped nasal cavity walls. The outer face of both species is included to account for realistic particle inhalation. This comparative study can contribute towards improving extrapolation from monitored exposures of laboratory animals to possible human exposure scenarios, and better understanding the cause-and-effect relationship between particle exposure risk and health consequences.

Methods

Nasal models

Computational models of the human (48-year-old healthy male) and rat (Sprague-Dawley, 400 g) nasal passages were developed based on CT images. The models were truncated at the anterior trachea to focus on particle deposition in the upper respiratory tract. Figure 1a shows the airway reconstructed from CT images. The models include both left and right nasal passages, and the nasopharyngeal duct. Detailed model reconstruction and its verification have been reported in the author's previous article (Inthavong et al., 2009). To better represent the flow conditions at and around the nostril inlets, the external nares, facial features, and the surrounding environment near the face were included (Figure 1b) (Doorly et al., 2008; Ge et al., 2013; Inthavong et al., 2012, 2013; King & Inthavong, 2010).

The nasal surface were divided into seven regions based on a combination of anatomical features and epithelial tissue types (Gross et al., 1982; Schroeter et al., 2012, 2015). These regions are: the (i) vestibule (squamous epithelium); (ii) upper passage (mainly transitional epithelium); (iii) middle and (iv) lower passage (mainly respiratory epithelium), (v) olfactory (olfactory epithelium), (vi) septum and (vii) pharynx.

The surface-mapping technique originally developed by Inthavong et al. (2014) was adopted to unwrap the nasal cavity morphology from its 3D domain (Figure 2a and b) onto a planar 2D domain and normalized its length and width (Figure 2c and d). The model was first sliced along the centerline of the nasal passage floor; where the lateral and septal wall sides meet inferiorly. The 3D surface coordinates were transformed into a new set of coordinates in 2D space, which mimics the surfaces being unfurled and laid out with the top and bottom boundaries representing the initial centerline slice along the nasal passage floor, and the left and right boundaries representing the nostril inlet, and nasopharynx exit respectively. Finally, the 2D surface was normalized into an orthogonal shape allowing direct comparisons between species.

The computational models were meshed using ICEM-CFD (ANSYS® Inc., Canonsburg, PA) with unstructured tetrahedral elements. Prism layers were applied in near wall regions to provide accurate near wall particle behavior. The number of independent mesh elements for the human and rat models were 3.8 million and 4.2 million, respectively.

Inhalation and particle deposition modelling

Physiological reasonable steady flow rates (15 L/min for the human model and 0.4 L/min for the rat model) are used to simulate rest breathing conditions (Kelly et al., 2004). The flow was treated as laminar and incompressible using the commercial CFD package, ANSYS-Fluent v14.5 (ANSYS®). To ensure similarity with particle exposure experiments, micron-sized particles were released in front of breathing zone (Figure 1b). It was reported that particle deposition fraction approaches 100% in human nasal cavities when particle diameters >20 μm (Inthavong et al., 2006), while for rats, this occurs for particle diameters >5 μm (Kelly et al., 2001b). Therefore, this study is mainly focused on particle diameter within the range of 0.5–20 μm for the human model and 0.5–5 μm for the rat model.

The particle Stokes number (Stk) was calculated to compare the different fluid–particle behavior caused by interspecies differences between the human and rat models. It is commonly used in respiratory deposition studies (Inthavong et al., 2011; Schroeter et al., 2012; Si et al., 2013; Wang et al., 2009) since it considers the flow rate, particle, and airway geometry, which all contribute towards the inertial character of the airborne micron particle. These variables come together as

$$Stk = \frac{\rho d^2 u_c}{18\mu d_c} \tag{1}$$

where ρ is the particle density, d is the particle diameter, u_c is the equivalent characteristic air velocity, μ is the fluid viscosity and d_c is the equivalent characteristic dimension of the nasal passage. Substituting airflow rate $Q = u_c \pi (\frac{1}{2} d_c)^2$, Equation (1) is transformed to:

$$Stk = \frac{2\rho d^2 Q}{9\pi \mu d_c^3} \tag{2}$$

The calculation of the Stk largely depends on a characteristic diameter d_c that is determined from the airway geometry, which wields significant influence. In this study, the characteristic diameter is estimated by the total nasal volume V and the total nasal surface area S (Garcia et al., 2009; Golshahi et al., 2011; Storey-Bishoff et al., 2008)
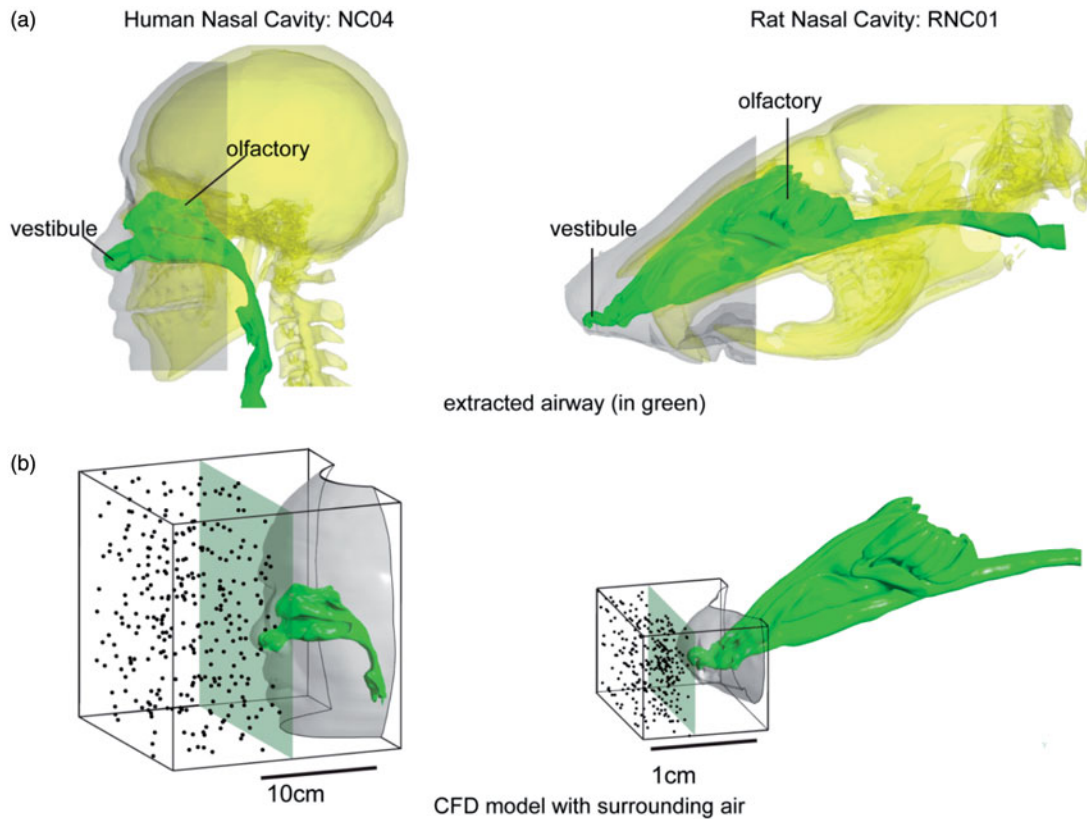
$$d_c = V/S \tag{3}$$

Figure 1. (a) Contiguous nasal airway passage (green) extracted from CT-scans. Additional anatomical features are overlaid in gray color for the outer face, and green color for bone structure. (b) CFD model showing the face-nasal cavity computational domain exposed to micron particles from the surrounding air. The human nasal cavity used in this study is labeled as NC04 and the rat nasal cavity is RNC01.
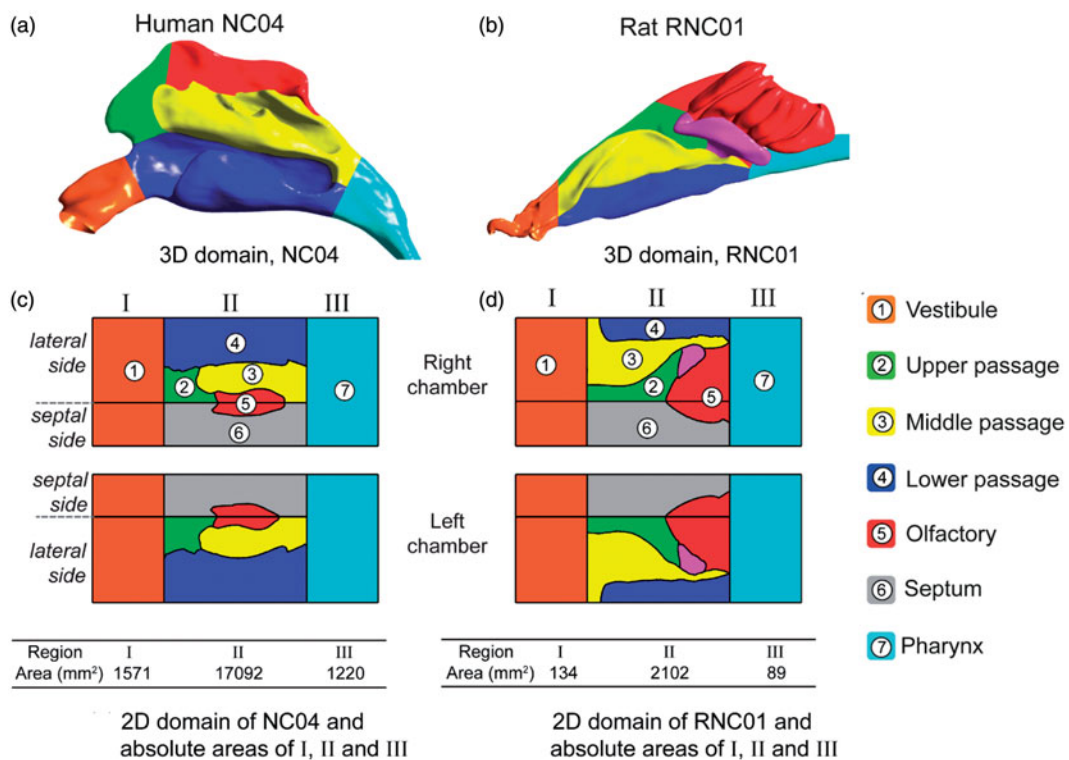

Figure 2. (a) and (b) 3D domain of the human nasal cavity and (c) and (d) 2D unwrapped models of the Human NC04 and Rat RNC01 nasal models separated, and labeled with seven major nasal anatomical types. As surfaces were significantly distorted in 2D domains during normalization, absolute surface areas of the vestibule (I), main passage (II) and pharynx (III) are given.

Table 1. Comparison of deposition fractions, particle sizes, inertial parameters and Stokes numbers for the rat and human models.

Inertial	Deposition fraction		Particle diameter (μm)		Inertial parameter $\rho d^2 Q$ (g μm^2/s)		Stokes No.	
	Rat (%)	Human (%)	Rat	Human	Rat	Human	Rat	Human
Low	3	3.4	1	2.5	6.7	1562.5	1.2	3.0
Medium	40	40	2	9	26.7	20250	4.8	39.0
High	100	100	3	20	60	100000	10.9	193.3

Table 2. Geometrical comparison of major anatomical regions for rat and human nasal models.

Region ID	Region name	Surface area of rat RNC01 (mm^2)	Percentage of surface area (%)		Surface area of human NC04 (mm^2)	Percentage of surface area (%)	
			Present model	Literature		Present model	Literature
1	Vestibule	134	5.8	4.4[a], 4.0[b], 3–4[c]	1571	7.9	8.2[a], 6.2[b]
2	Upper passage	119	5.1		566	2.8	
3	Middle passage	241	10.3		5343	26.9	
4	Lower passage	140	6.0		5147	25.9	
5	Olfactory	1294	55.6	41.8[a], 40.6[d], 50–52[c]	2097	10.5	9.5[a]
6	Septum	308	13.3		3939	19.9	
7	Pharynx	89	3.9		1220	6.1	
Total area (mm^2)		2325	100		19882	100	
		Rat NC04			Human NC04		
Nasal volume (mm^3)		653.2			25267.4		
Characteristic length d_c (mm)		0.28			1.27		

[a]Schroeter et al. (2008).
[b]Schroeter et al. (2014).
[c]Gross et al. (1982).
[d]Garcia and Kimbell (2009).

Typical low, medium and high inertial particles were defined according to their total deposition fractions ∼3, 40 and 100 in the human and rat nasal cavities. The corresponding particle sizes are 2.5, 9 and 20 μm for the human model, and 1, 2 and 3 μm for the rat model. However, the corresponding Stokes numbers are quite different, with 3.0, 39.0 and 193.3 for human and 1.2, 4.8 and 10.9 for rat (Table 1).

Particle deposition visualisation

Previous studies have demonstrated that particles deposit on the skin-like squamous epithelium in the vestibule region can be cleared from the nose, and those enter into nasopharynx region are likely to deposit in lower respiratory tract therefore damaging the lung (Schroeter et al., 2008). Three main nasal areas (Figure 2) were defined to evaluate and compare the nasal filtering function for all three typical particles. These areas are: area-I (includes the nasal vestibule); area-II (includes the main nasal passage) and area-III (includes the nasopharynx).

Although regional particle deposition fraction analysis have been extensively investigated in previous studies (Schroeter et al., 2008, 2015; Garcia & Kimbell, 2009), direct interspecies comparisons remains difficult due to the inconsistency during the anatomical region mapping, geo-metrical variations of nasal models and significant anatomy differences between human and rat nasal models. To allow direct comparisons, we visualize the particle deposition pattern across the entire nasal cavity surface using the unwrapped surface technique.

The particle deposition pattern was visualized using 10 000 particle deposition locations on the 3D transparent nasal domain (side view and top view), and the corresponding unwrapped 2D domain. In addition, cross-sectional particle densities were extracted along the nasal passage to reflect the deposition depth of hot spots. Therefore, particle deposition hot spots can be visualized in 3D, 2D and 1D, which enables an effective way to distinguish different sized particle deposition patterns and quantify the particle deposition penetration.

Results and discussion

Nasal cavity measurements and comparison

Anatomical measurements of the major epithelial regions were compared between the human and rat models in Table 2. The total surface area of the human model was almost 10 times of the rat model. The largest surface area coverage for the human model were the middle (26.9%) and lower passages (25.9%) which combined together to make up approximately 52.8% of the total surface area. In contrast, the rat middle and lower passage only took up 16.3% in total. The largest area coverage for the rat model was the olfactory region which contributes 55.6%, enabling the region to have greater exposure to inhaled particles. This compared with the human model that showed a value of 10.5%.

Comparisons with available data from literature were made for the vestibule and olfactory regions. There is generally good agreement for the human and rat model based on the epithelia mapping. The rat vestibule and olfactory region is slightly greater than the reported values in the literature.
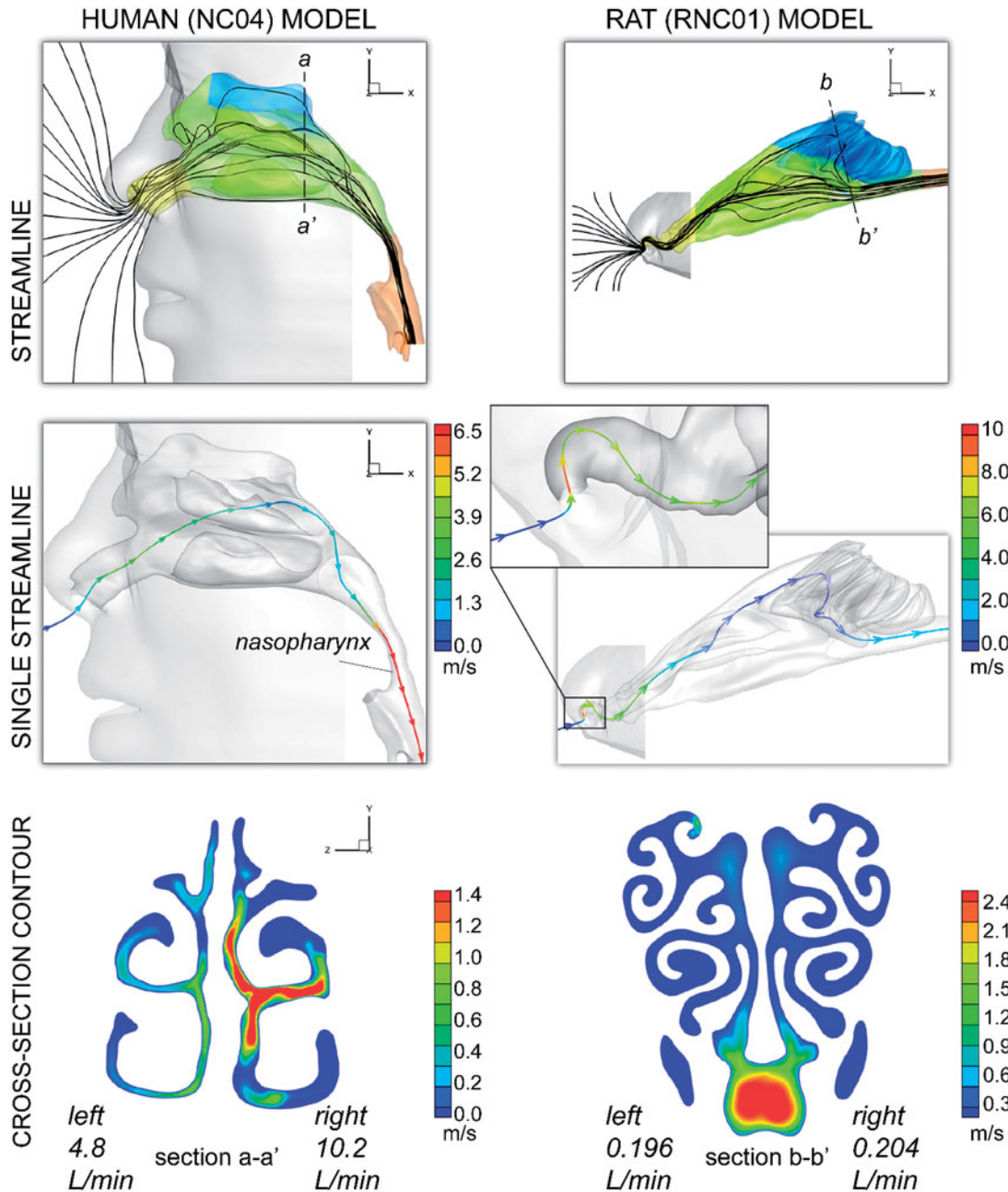
Figure 3. Representative flow streamlines in the human, and rat nasal cavities showing regions of high velocity. A cross-section slice taken at a–a′ in the human model and b–b′ in the rat model shows velocity magnitude contours.

These two regions were selected for comparison as they have important roles in basic nasal functions. As the most anterior part of nasal cavity, the vestibule is covered by vibrissae (short and thick hairs), enhancing particle filtration while the olfactory region is rich in olfactory sensory neurons and capillaries, allowing olfaction. The nasal volume of the human model is 39 times of the rat model. However, the characteristic length of human model (1.27 mm) is only around five times of the rat model (0.28 mm), indicating that the nasal structure of rat is more complex than that of human (Table 2).
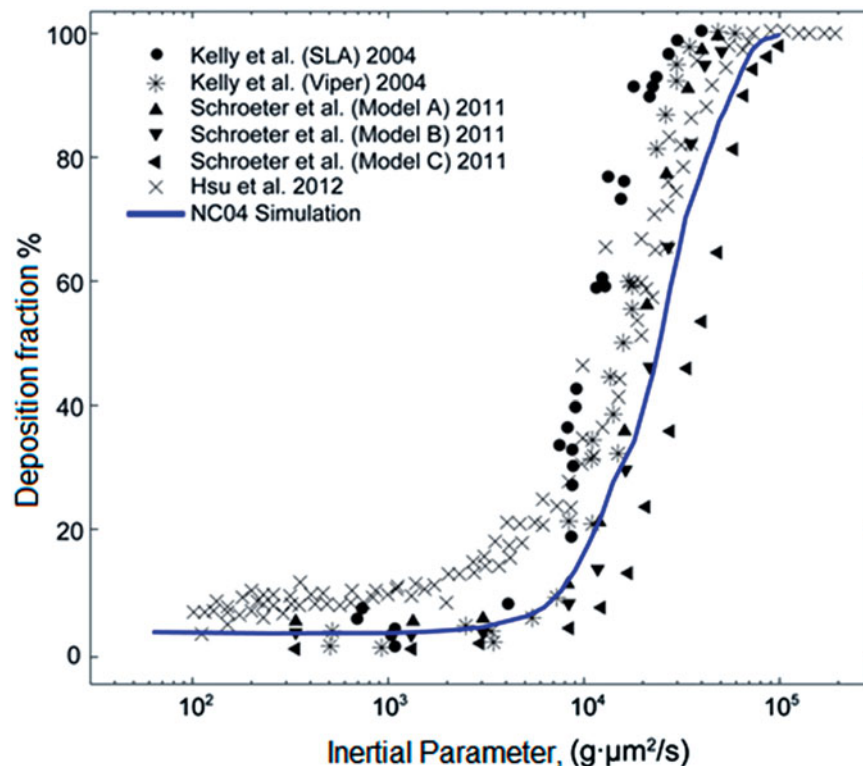
Inhalation flow patterns

Tracing flow streamlines provides insight to the likely path trajectory an airborne particle may follow. Flow streamlines

were traced from the outside air as it enters the nostril inlet (Figure 3). By including the facial features, natural flow paths are produced (Corley et al., 2012; Doorly et al., 2008) which differs to cast replica model studies or computational models that omit the face and outside air region.

For the human model, the streamlines predominantly distribute through the center rather than the ceiling or the floor of the airway. Swirling flow is found near the olfactory region and this can be attributed to the lower flow velocities found in the upper airway region to allow gases to be taken up by olfactory nerves, but prevent larger micron-sized particles from reaching the nerves and damaging them. The single streamline shows flow acceleration immediately after the nostril inlet, and high acceleration at the nasopharynx caused by the airway passage decreasing to a smaller cross-sectional area. These regions of acceleration propel the airborne

Figure 4. Particle deposition fraction as a function of the inertial parameter I comparison between the results obtained from the human NC04 model simulation with data in the literature.

Particle deposition fraction comparison

The particle deposition fraction was defined as the ratio of the number of particles depositing in the nasal cavity to the total amount of particles inhaled. This was plotted against the particle inertial parameter $I = \rho d^2 Q$ where ρ is the particle density (g/cm^3), d is the particle diameter (μm) and Q is the volume flow rate (cm^3/s). Comparisons were made with existing literature data to confirm the reliability of the computational model simulations.

Figure 4 compares the simulation results for the human NC04 model with: *in vitro* data from Kelly et al. (2004) that used a human nasal replica made from MRI scans of a Caucasian male subject; CFD simulations by Schroeter et al. (2011) that modified Kelly et al. (2004)'s model into model A, B and C with three different surface roughness; and *in vivo* data by Hsu & Chuang (2012) that studied nine male and female volunteers from Taiwan with ages ranging from 23 to 45. The predicted deposition fraction profile produced an S-shaped inertial deposition curve and showed good agreement with the existing data; especially well matched with Model B from Schroeter et al. (2011). The deposition fraction remains <10% when the inertial parameter $I < 10^4$ g·μm^2/s. As the inertial parameter I increases, the deposition profile increases sharply and reaches complete deposition when $I > 10^5$ g·μm^2/s.

Figure 5 compares the simulation results for the rat RNC01 model with: *in vivo* data from Kelly et al. (2001a) that studied particle exposure experiments on 22 female Long-Evans rats; and *in vitro* data from Kelly et al. (2001b) using a nasal replica cast model from one Long-Evans rats. The comparison shows that for inertial parameter $I < 10$ g·μm^2/s, the numerical simulation slightly under predicts with the *in vivo* results (triangle symbols) but fits better with the *in vitro*

particles forwards, increasing the particle inertia. This increases the likelihood of particle impaction when the flow streamline changes path and the particle inertia is too great. This flow feature makes the anterior nasal half and the nasopharynx region acting as a gravimetric sampling filter. The cross section shows a flow preference to the left nasal chamber which is caused by the larger volume found from the scanned data, linked to the regulating nasal cycle.

For the rat model flow enters the nose and immediately turns sharply, followed with a U-shaped turn and a further 90° bend before entering the main nasal passage. These sharp turns provides significant filtration function. The initial sharp acceleration increases the velocity from the ambient zero velocity to 10 m/s in the space of a few millimeters. In the human model, the acceleration in the nostril region increases the velocity to 2.5 m/s and in the nasopharynx increases to 6.5 m/s. The rapid velocity increase over a short distance in the rat airway significantly increases the particle deposition for micron-sized particles. This has significant implications when direct comparisons are made for deposition models with human nasal cavity airways that have a more relaxed acceleration through the nasal vestibule.

Although the olfactory regions of both human and rat are located in the dorso-posterior region, the olfactory region of human is located superiorly relative to the nostril entry for inhaled air while the rat model it is in-line with the nostril entry. For the rat model particles or gases that are able to penetrate the anterior nose are easily taken up by the olfactory region, particularly since the region has 50% surface coverage of the entire nasal cavity. The cross-section slice shows the rat passage has a more complicated geometry. The flow concentrated along the floor of the airway and this is because the lower region connects to the pharynx.

Figure 5. Particle deposition fraction as a function of the inertial parameter I comparison between the results obtained from the human RNC01 model simulation with data in the literature.
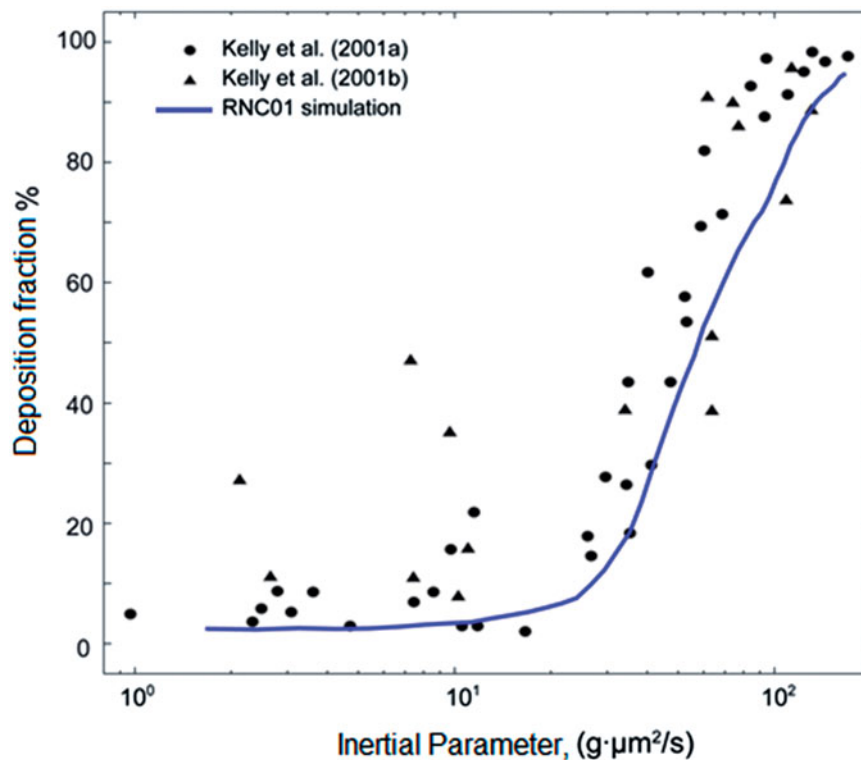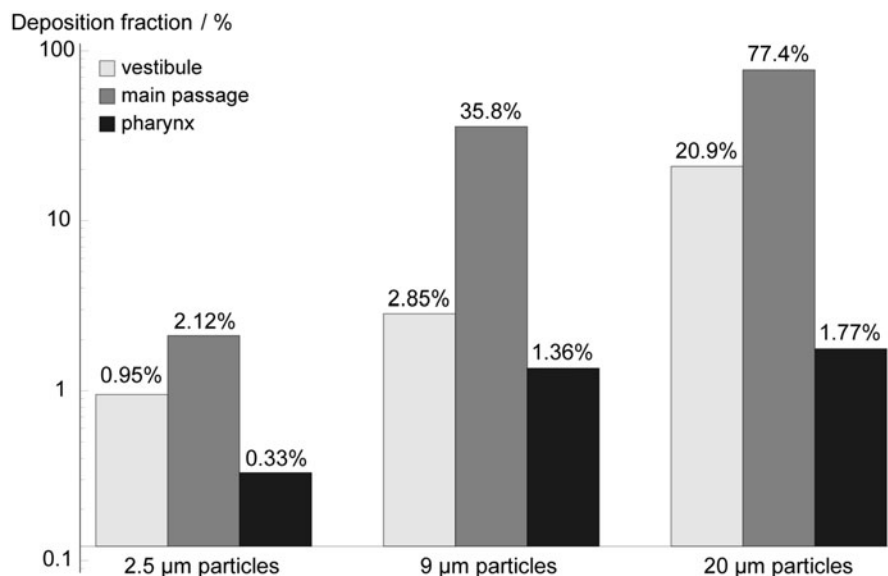

Figure 6. Regional particle deposition fraction comparison for the human NC04 model using semi-log axes.

results (circle symbols). For inertial parameter $I > 10 \text{ g} \cdot \mu\text{m}^2/\text{s}$, the numerical model compares well for both experimental results with a slight under prediction when inertial parameter I approaches $10^2 \text{ g} \cdot \mu\text{m}^2/\text{s}$.

Deposition in the human NC04 model

Figure 6 shows a majority of particles depositing in the main nasal passage (II) capturing 2.12, 35.8 and 77.4% of particles for the low, medium and high inertial, respectively. Preferential deposition in this region occurs because the airway opens up from the anterior nose allowing more particles to access the main passage. Although the vestibule is the second preferred deposition site, the deposition fractions are negligible for low (0.95% deposition) and medium (2.85% deposition) inertial particles. It increases significantly to 21% for high inertial particles. The nasopharynx (III) region has the lowest deposition for all particle sizes due to its posterior location.

Figure 7 shows the deposition pattern in the human NC04 model. Deposition of 2.5 μm particles shows a large, widely dispersed deposition pattern with a total deposition fraction of 3.5% (left chamber: 1.1%, right chamber: 2.4%). The deposition pattern in 3D space is cast onto the 2D domain
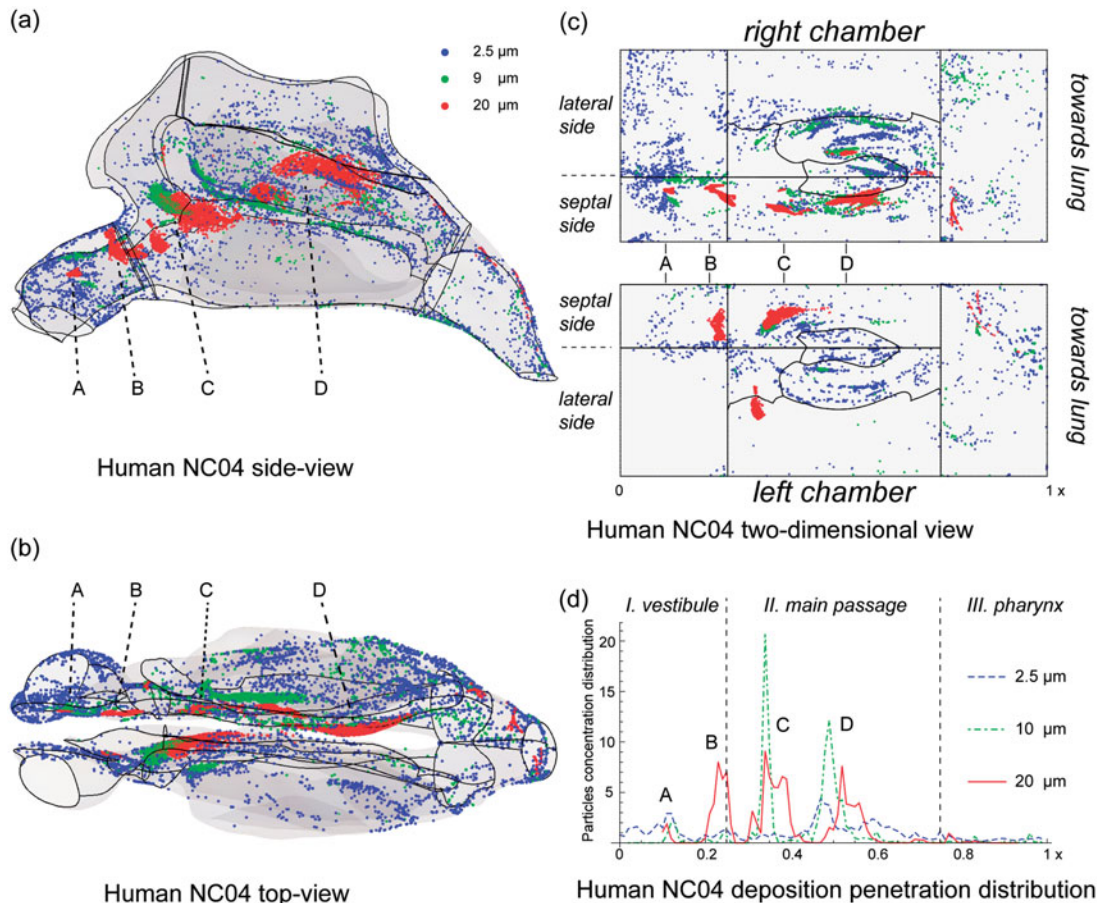
Figure 7. Particle deposition patterns for the human NC04 model in the 3D domain (a and b), 2D planar domain (c) and deposition penetration distribution (d). Particle sizes are colored based on the low (2.5 μm, blue), medium (9 μm, green) and high inertial (20 μm, red) according to their deposition fractions reported. The *x*-coordinate in (d) is normalized by the maximum penetration depth from nostril to naso-pharynx.

which reveals the extent of dispersion (Figure 7c). This is characteristic of low inertial particles that are more likely to adapt to the changing inhaled flow paths as it is being transported through the nasal cavity and penetrate the nasal cavity further. For a particle size of 9 μm, the total deposition fraction is 40.0% (left chamber: 17.7%, right chamber: 22.3%) as the particle inertia is increased. This leads to fewer particles able to follow the airflow, and its deposition pattern region reduces. For 20 μm particles, deposition fraction reaches 100% with a majority 70% depositing in the right chamber. Particles are mainly concentrated in the main nasal passage (area II) by direct impaction. The deposition pattern cast onto the 2D domain shows local concentration of particles near the entrance to the main nasal passage. In both cavities, deposition occurs on the nasal septal wall side. More particles deposited in the right chamber compared to the left chamber for all three particle sizes tested. This was mainly due to the asymmetric geometry of the human NC04 model, where its right nasal chamber is slightly larger than the left, allowing more airflow through with less flow resistance (which was found in the cross section contour in Figure 3). We analyzed the mass flow attribution in each chamber which showed a 32:68% flow rate distribution in the left to right chambers. Figure 7© shows particle deposition is more disperse and broad in the right cavity compared to the left cavity. One major reason is the degree of the uneven flow

rates between the two chambers producing irregular path trajectories. Particles prefer to deposit at sites where the airflow velocity decreases sharply. This is consistent with the cross-sectional contour of the human model in Figure 3 (bottom-left panel) where the airflow in the right cavity exhibits much higher velocity gradient than that in the left cavity, causing particles to scatter more around the cavity.

The deposition penetration distribution in Figure 7(d) indicates that particles are concentrated in four hot spots labeled as ''A'', ''B'', ''C'' and ''D'' in the human nasal cavity. Location ''A'' and ''D'' are located at the top of vestibule of right cavity and posterior septum of right cavity, respectively. These regions in the right chamber are preferential deposition sites for all three particles. Further inspection of the geometry shows that region is a consequence of the airflow entering the nostril inlet at higher momentum, while location ''D'' exhibits a minor deviated septum causing flow disturbance.

Location ''B'' has high deposition of high inertial particles (20 μm) only for both chambers. This location is located at the ''nasal valve'' which is close to the common boundary of vestibule and septum of both cavities. Location ''C'' exhibits high deposition for medium (9 μm) and high (20 μm) inertial particles. The deposition occurs at the anterior septum for both chambers and at the common boundary of septum and upper passage of left cavity.

Figure 8. Regional particle deposition fraction comparison for the rat RNC01 model using semi-log axes.
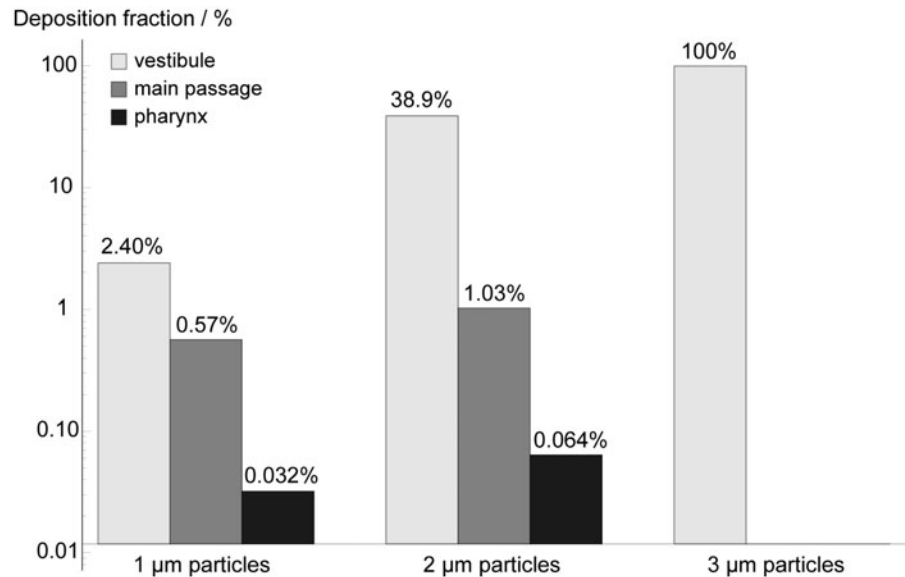
Rat RNC01 model

Local deposition fractions for the rat model (Figure 8) exhibit a different profile to the human model. For all particles, deposition predominantly occurs in the vestibule (I) region with deposition fractions of 2.4, 38.9 and 100% for the low, medium, and high particle inertial, respectively. This suggests that the region behaves as a significant particle filter. This correlates with the anatomy which shows highly curved and narrowing vestibules that accelerate the air from stagnant velocity to a peak of 10 m/s within the curved vestibule. The influence on a 3 μm particle is profound displaying complete inertial impaction at the nostril bend, thus offering a good protection for the olfactory region and the lung.

The high velocity combined with the small airway geometry in the rat model produces highly sensitive behavior for incremental changes in particle size. When the particle size reduces from 3 μm to 2 μm the deposition fraction decreases from 100 to 40% and a further reduction to 1 μm produces only 3% deposition. The implication is that experimental rat studies become highly susceptible to variability in the controlling the production of monodispersed particles for exposure. In this study using the rat model RNC01, particles spanning a few microns in size exhibit vastly different deposition behavior. The micron particle size range sensitivity will increase further in general if the peak velocity is greater, and the airway geometry is smaller. Conversely the size range will be greater when the peak velocity is smaller and the airway geometry is generally larger, as found for the human model NC04.

The deposition patterns for the rat RNC01 model (Figure 9) showed significant differences to those in the human model. The majority of high (3 μm) and medium (2 μm) inertia particles deposited at the sharp bend of the nasal vestibule, and only the finest 1 μm particles penetrated and dispersed through the main nasal passages. This is primarily due to the rapid acceleration of air as it enters the nose which is then confronted with two curvatures in the airway resembling an 180° bend and a 90° bend.

This anatomical feature creates a natural filtering function, trapping inertial particles on the upper wall of the nostril bend. This is exemplified by deposition of the 3 μm particles occurring on the upper wall of the nostril bend, and the 2 μm particles depositing across the narrow radial strip around the nostril inlet. For 1 μm particles a more distributed pattern occurs through the nasal cavity, although this also exhibits a preference for the nostril inlet region. Schroeter et al.'s (2012) simulations indicated particles do not achieve 100% deposition fraction until particle sizes reach 5 μm, which is much larger than the 3 μm found in this study. We believe this is due to the larger Sprague-Dawley rat size used in Schroeter et al. (2012), which had a weight 50% heavier than the rat used in this study. A larger specimen would have wider nasal passages, allowing slower velocity magnitude and lower resistances.

The deposition penetration distribution in Figure 9(d) shows three high concentration spots (''A'', ''B'' and ''C'') which are all located at the vestibule region. The 3 μm particles have direct impaction concentrated at upper region of the first nostril bend (location ''A'') when inhaled into nostrils with high-speed airflow. With lower inertia, 2 μm particles penetrate slightly further and deposit on the lateral wall (location ''B'') located between the first and second nostril bends. Although 1 μm particles pass through the first bend, the majority of them are captured at the second bend at location ''C''. Apart from the vestibule, the olfactory region also exhibits some significant deposition (location ''D'') but this only occurs for 1 μm particles.

A comparison of the deposition fractions for the low, medium and high inertial particles shows reasonably consistent values between the rat and human models. The deposition fraction is highly sensitivity to particle size for rats as there is a jump from 3 to 100% for an increase from 1 to 3 μm particles. In comparison, the same increase in deposition fraction in the human model occurs from a particle size of 2.5 to 20 μm. The rat airway geometry is relatively symmetric in this RNC01 model. The cross sectional contour in Figure 3
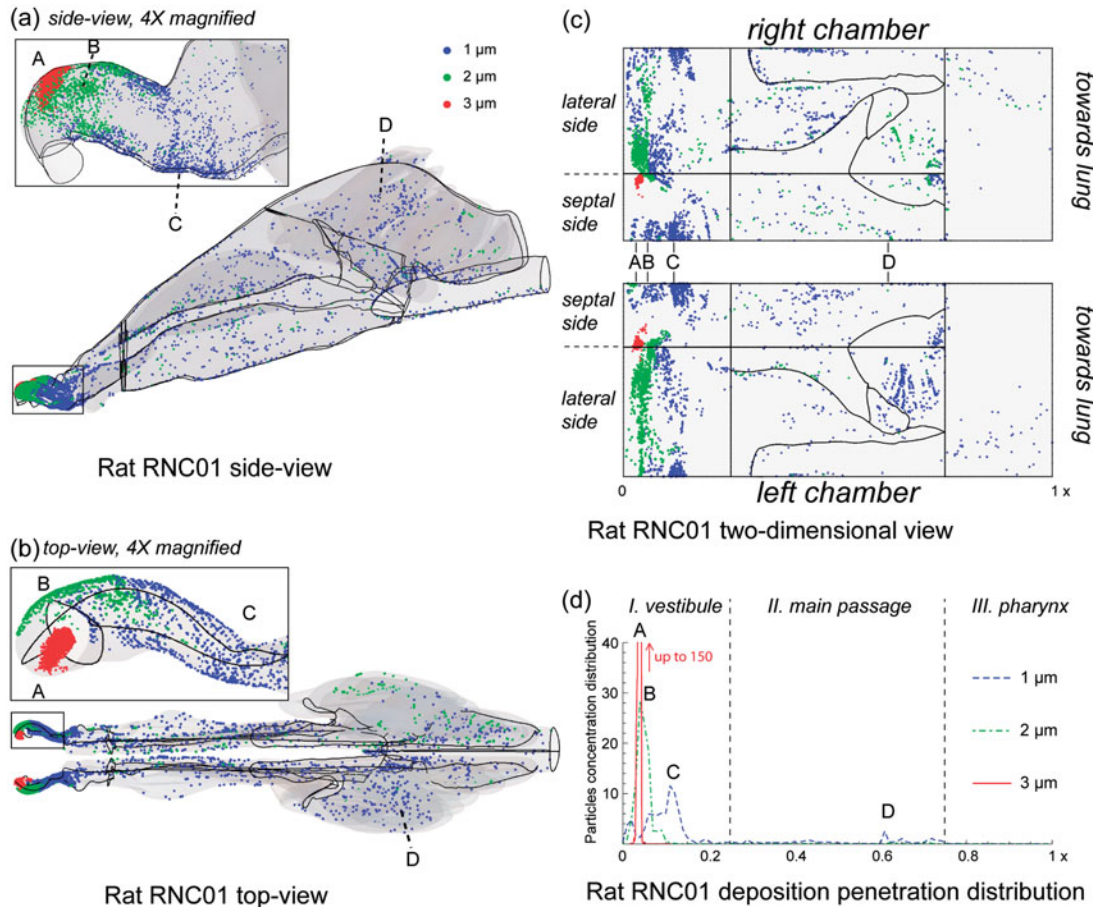
Figure 9. Particle deposition patterns for the rat RNC01 model in the 3D domain (a and b), 2D planar domain (c) and deposition penetration distribution (d). Particle sizes are colored based on the low (1 μm, blue), medium (2 μm, green) and high inertial (3 μm, red) according to their deposition fractions reported. The *x*-coordinate in (d) is normalized by the maximum penetration depth from nostril to naso-pharynx.

Table 3. Comparison of particle deposition dose-metric (deposition per unit area) between rat and human.

Inertial	Low			Medium			High		
Region names	*f* (rat)	*f* (human)	Scaling factor	*f* (rat)	*f* (human)	Scaling factor (*X*)	*f* (rat)	*f* (human)	Scaling factor (*X*)
Vestibule	0.42	0.12	0.29	6.8	0.46	0.068	17	2.1	0.12
Upper passage	0.0035	0.0056	1.6	0.013	0.0024	0.18	0	0	N/A
Middle passage	0.012	0.039	3.3	0.016	0.9	56	0	0.32	N/A
Lower passage	0.009	0.01	1.1	0.0082	0.047	5.7	0	0.15	N/A
Olfactory	0.0045	0.004	0.89	0.011	0.035	3.2	0	0.13	N/A
Septum	0.0082	0.017	2.1	0.012	0.98	82	0	2.4	N/A
Pharynx	0.0073	0.053	7.3	0.015	0.26	17	0	0.25	N/A

Particle deposition flux *f*: Regional deposition fraction/regional area fraction.

shows ∼0.2 L/min air flow through each chamber, which produced nearly equal amounts of particle deposition in both chambers.

Extrapolation from rat to human

We calculate the deposition fraction in the seven anatomical/epithelial tissue regions defined in Figure 2. The deposition fraction is then normalized by the regional area fraction (which is simply the regional area divided by the total surface area). This creates a deposition flux value and can be written as

$$f = \frac{n_{regional}/n_{total}}{A_{regional}/A_{total}}$$

Where $n_{regional}$ is the quantity of particles deposit in a particular region and n_{total} is the quantity of particles inhaled into the nasal cavity. $A_{regional}$ is the regional area and A_{total} is the total nasal surface area.

Table 3 summarizes the deposition flux for the human and rat model to evaluate the possible deposition extrapolation for low, medium and high inertial particles. In general, for all particles, highest *f* value is found in the vestibule region. While the upper passage typically exhibits the lowest deposition flux. To enable direct deposition data extrapolation, regional scaling factor is introduced as the variations between the rat and human models are not linear for each region. Scaling factors *X* are calculated based on the ratio of the *f* of the human model to the rat model. The values show

that direct extrapolation is not applicable for high inertial particles since no particles with size 3 μm or greater can penetrate the rat vestibule. The maximum scaling factor ($X = 82$) occurs in the septum region for medium inertial particles. This is mainly attributes to the medium inertial particles can travel deeper downstream in the human nasal model, while majority of them are filtered by the vestibule region for the rat model. Similarly, due to this efficient filtration, the vestibule shows a minimum scaling factor ($X = 0.068$) for medium inertial particles. For low inertial particles, upper passage, lower passage and olfactory regions exhibit the closest 1:1 matching for data extrapolation.

Conclusion

Results obtained from exposure studies using rat models are typically extrapolated to human subjects. The objective of this study was to gain further insight for extrapolating inhalation exposure data between inter-subject species. The anatomy, airflow, and particle deposition in a rat and human nasal cavity was investigated using CFD. Anatomy comparisons showed that the cavity surface area of the human model was about ten times the size of the rat. The largest surface area coverage for the human was the middle and lower passages which combined to make up 52.8% of the total surface area, while for the rat model, the olfactory region made up 55.6% of the total surface area. These regions were also the preferential sites for deposition of 2.5 μm particles. The other major anatomical difference is the shape of the nasal vestibule which plays a significant role in producing the inhaled airflow streamlines. A sharp U-turn (180°) bend is found in the rat model which accelerates the inhaled air to a peak velocity of 10 m/s despite an inhalation rate of 0.4 L/min. Comparatively the human model exhibits a 90° bend at the nasal vestibule and accelerates the flow to 2.5 m/s for an inhalation rate of 15 L/min. To account for these differences we used the total deposition fraction to determine appropriate particle sizes for low, medium, and high inertial properties. It was found that the particle size range suitable to represent these three inertial regimes was 2.5 to 20 μm for the human model and 1 to 3 μm for the rat model. This places stringent limitations for particle size selections for rat inhalation exposure studies. We introduced a deposition flux parameter which compares the deposition fraction per regional area fraction for the human and rat models. A direct comparison showed that a scaling factor was needed in order to extrapolate the deposition data from one species to another. Low inertial particles show the closest scaling factor of 1:1 matching. Although this study only investigated a single subject specific model for rat and human species, the key anatomical differences and deposition pattern is expected to be reasonably common across different models.

Acknowledgements

Declaration of interest

References

Ahmed A, Prime D, Burnell PKP, Hogger P. (2012). Development of an *in vitro* model to assess deposition of aerosol particles in a representative replica of the rat's respiratory tract. J Aerosol Med Pulm Drug Deliv 25:169–78.

Asgharian B, Price OT, Oldham M, et al. (2014). Computational modeling of nanoscale and microscale particle deposition, retention and dosimetry in the mouse respiratory tract. Inhal Toxicol 6:829–42.

Bai R, Zhang L, Liu Y, et al. (2010). Pulmonary responses to printer toner particles in mice after intratracheal instillation. Toxicol Lett 199:288–300.

Cheng K, Cheng Y, Yeh H, et al. (1996). *In vivo* measurements of nasal airway dimensions and ultrafine aerosol deposition in the human nasal and oral airways. J Aerosol Sci 27:785–801.

Cheng Y, Hansen G, Su Y, et al. (1990). Deposition of ultrafine aerosols in rat nasal molds. Toxicol Appl Pharmacol 106:222–33.

Corley RA, Kabilan S, Kuprat AP, et al. (2012). Comparative computational modeling of airflows and vapor dosimetry in the respiratory tracts of rat, monkey, and human. Toxicol Sci 128:500–16.

Dai YT, Chang CP, Tu LJ, Hsu DJ. (2007). Development of a Taiwanese head model for studying occupational particle exposure. Inhal Toxicol 19:383–92.

Dastan A, Abouali O, Ahmadi G. (2014). CFD simulation of total and regional fiber deposition in human nasal cavities. J Aerosol Sci 69: 132–49.

Doorly DJ, Taylor DJ, Schroter RC. (2008). Mechanics of airflow in the human nasal airways. Respir Physiol Neurobiol 163:100–10.

Garcia GJM, Kimbell JS. (2009). Deposition of inhaled nanoparticles in the rat nasal passages: dose to the olfactory region. Inhal Toxicol 21: 1165–75.

Garcia GJM, Tewksbury EW, Wong BA, Kimbell JS. (2009). Interindividual variability in nasal filtration as a function of nasal cavity geometry. J Aerosol Med Pulm Drug Deliv 22:139–55.

Ge Q, Li X, Inthavong K, Tu J. (2013). Numerical study of the effects of human body heat on particle transport and inhalation in indoor environment. Building Environ 59:1–9.

Gerde P, Cheng Y, Medinsky M. (1991). *In vivo* deposition of ultrafine aerosols in the nasal airway of the rat. Fundam Appl Toxicol 16: 330–6.

Ghahramani E, Abouali O, Emdad H, Ahmadi G. (2014). Numerical analysis of stochastic dispersion of micro-particles in turbulent flows in a realistic model of human nasal/upper airway. J Aerosol Sci 67: 188–206.

Ghalati P, Keshavarzian E, Abouali O, et al. (2012). Numerical analysis of micro- and nano-particle deposition in a realistic human upper airway. Comput Biol Med 42:39–49.

Golshahi L, Noga ML, Thompson RB, Finlay WH. (2011). In vitro deposition measurement of inhaled micrometer-sized particles in extrathoracic airways of children and adolescents during nose breathing. J Aerosol Sci 42:474–88.

Gross EA, Swenberg JA, Fields S, Popp JA. (1982). Comparative morphometry of the nasal cavity in rats and mice. J Anatomy 135: 83–8.

Hsu DJ, Chuang MH. (2012). In-vivo measurements of micrometer-sized particle deposition in the nasal cavities of Taiwanese adults. Aerosol Sci Technol 46:631–8.

Inthavong K, Ge QJ, Li A, Tu JY. (2013). Source and trajectories of inhaled particles from a surrounding environment and its deposition in the respiratory airway. Inhal Toxicol 25:280–91.

Inthavong K, Ge QJ, Li XD, Tu JY. (2012). Detailed predictions of particle aspiration affected by respiratory inhalation and airflow. Atmospheric Environ 62:107–17.

Inthavong K, Shang YD, Tu JY. (2014). Surface mapping for visualization of wall stresses during inhalation in a human nasal cavity. Respir Physiol Neurobiol 190:54–61.

Inthavong K, Tian ZF, Li HF, et al. (2006). A numerical study of spray particle deposition in a human nasal cavity. Aerosol Sci Technol 40:1034–45.

Inthavong K, Tu JY, Ahmadi G. (2009). Computational modelling of gas-particle flows with different particle morphology in the human nasal cavity. J Computat Multiphase Flows 1:57–82.

Inthavong K, Tu JY, Heschl C. (2011). Micron particle deposition in the nasal cavity using the v(2)-f model. Computers Fluids 51:184–8.

Inthavong K, Wen J, Tian ZF, Tu JY. (2008). Numerical study of fibre deposition in a human nasal cavity. J Aerosol Sci 39:253–65.

Jiang J, Zhao K. (2010). Airflow and nanoparticle deposition in rat nose under various breathing and sniffing conditions: a computational evaluation of the unsteady effect: computational of unsteady turbulent. J Aerosol Sci 41:1030–43.

Kelly J, Bobbitt C, Asgharian B. (2001a). *In vivo* measurement of fine and coarse aerosol deposition in the nasal airways of female Long-Evans rats. Toxicol Sci 64:253–8.

Kelly J, Kimbell J, Asgharian B. (2001b). Deposition of fine and coarse aerosols in a rat nasal mold. Inhal Toxicol 13:577–88.

Kelly JT, Asgharian B, Kimbell JS, Wong BA. (2004). Particle deposition in human nasal airway replicas manufactured by different methods. Part I: inertial regime particles. Aerosol Sci Technol 38:1063–71.

Kelly JT, Asgharian B, Wong BA. (2005). Inertial particle deposition in a monkey nasal mold compared with that in human nasal replicas. Inhal Toxicol 17:823–30.

Kelly JT, Tewksbury EW, Wong BA, Asgharian B. (2002). Nasal and lung deposition of fine and coarse particles in rats. Annals Occupat Hygiene 46:346–9.

King SE, Inthavong CM, Tu KJ. (2010). Inhalability of micron particles through the nose and mouth. Inhal Toxicol 22:287–300.

Oberdorster G, Sharp Z, Atudorei V, et al. (2004). Translocation of inhaled ultrafine particles to the brain. Inhal Toxicol 16:437–45.

Oldham MJ. (2000). Computational fluid dynamic predictions and experimental results for particle deposition in an airway model. Aerosol Sci Technol 32:61–71.

Schroeter J, Kimbell J, Asgharian B, et al. (2012a). Computational fluid dynamics simulations of submicrometer and micrometer particle deposition in the nasal passages of a Sprague-Dawley rat. J Aerosol Sci 43:31–44.

Schroeter JD, Campbell J, Kimbell JS, et al. (2014). Effects of endogenous formaldehyde in nasal tissues on inhaled formaldehyde dosimetry predictions in the rat, monkey, and human nasal passages. Toxicol Sci 138:412–24.

Schroeter JD, Garcia GJM, Kimbell JS. (2011). Effects of surface smoothness on inertial particle deposition in human nasal models. J Aerosol Sci 42:52–63.

Schroeter JD, Kimbell JS, Gross EA, et al. (2008). Application of physiological computational fluid dynamics models to predict interspecies nasal dosimetry of inhaled acrolein. Inhal Toxicol 20:227–43.

Schroeter JD, Tewksbury EW, Wong BA, Kimbell JS. (2015). Experimental measurements and computational predictions of regional particle deposition in a sectional nasal model. J Aerosol Med Pulm Drug Deliv 28:20–9.

Si XHA, Xi JX, Kim J, et al. (2013). Modeling of release position and ventilation effects on olfactory aerosol drug delivery. Respir Physiol Neurobiol 186:22–32.

Storey-Bishoff J, Noga M, Finlay WH. (2008). Deposition of micrometer-sized aerosol particles in infant nasal airway replicas. J Aerosol Sci 39:1055–65.

Wang SM, Inthavong K, Wen J, et al. (2009). Comparison of micron- and nanoparticle deposition patterns in a realistic human nasal cavity. Respir Physiol Neurobiol 166:142–51.

Wei ZH, Xu ZX, Li B, Xu FQ. (2013). Numerical simulation of airway dimension effects on airflow patterns and odorant deposition patterns in the rat nasal cavity. PLoS One 8:e770570. doi:10.1371/journal.pone.0077570.

Wolff R, Kanapilly G, Gray R, Mcclellan R. (1984). Deposition and retention of inhaled aggregate $^{67}Ga_2O_3$ particles in beagle dogs, Fischer-344 rats, and CD-1 mice. Am Ind Hyg Assoc J 45:377–81.

Zhao K, Dalton P, Yang GC, Scherer PW. (2006). Numerical modeling of turbulent and laminar airflow and odorant transport during sniffing in the human and rat nose. Chem Senses 31:107–18.